



When beauty is only skin deep; optimizing the sensitivity of specular neutron reflectivity for probing structure beneath the surface of thin films

Charles F. Majkrzak, Elisabeth Carpenter, Frank Heinrich, and Norman F. Berk

Citation: *J. Appl. Phys.* **110**, 102212 (2011); doi: 10.1063/1.3661979

View online: <http://dx.doi.org/10.1063/1.3661979>

View Table of Contents: <http://jap.aip.org/resource/1/JAPIAU/v110/i10>

Published by the [American Institute of Physics](http://www.aip.org).

Related Articles

Electrochemical cell for neutron reflectometry studies of the structure of ionic liquids at electrified interface
Rev. Sci. Instrum. **81**, 074101 (2010)

Surface force confinement cell for neutron reflectometry studies of complex fluids under nanoconfinement
Rev. Sci. Instrum. **79**, 103908 (2008)

Millisecond time resolution neutron reflection from a nematic liquid crystal
Rev. Sci. Instrum. **75**, 2955 (2004)

Adsorption from alkane+perfluoroalkane mixtures at fluorophobic and fluorophilic surfaces. I. Nature of the noncritical adsorption profiles
J. Chem. Phys. **119**, 11917 (2003)

Local membrane ordering of sponge phases at a solid–solution interface
J. Chem. Phys. **116**, 8533 (2002)

Additional information on *J. Appl. Phys.*

Journal Homepage: <http://jap.aip.org/>

Journal Information: http://jap.aip.org/about/about_the_journal

Top downloads: http://jap.aip.org/features/most_downloaded

Information for Authors: <http://jap.aip.org/authors>

ADVERTISEMENT

LakeShore Model 8404 developed with
TOYO Corporation
NEW AC/DC Hall Effect System Measure mobilities down to 0.001 cm²/V s

When beauty is only skin deep; optimizing the sensitivity of specular neutron reflectivity for probing structure beneath the surface of thin films^{a)}

Charles F. Majkrzak,^{1,b)} Elisabeth Carpenter,^{1,2} Frank Heinrich,^{1,3} and Norman F. Berk¹

¹*NIST Center for Neutron Research, Gaithersburg, Maryland 20899, USA*

²*Physics Department, New York University, New York, New York 10012, USA*

³*Physics Department, Carnegie Mellon University, Pittsburgh, Pennsylvania 15213, USA*

(Received 1 October 2010; accepted 15 February 2011; published online 30 November 2011)

Specular neutron reflectometry has become an established probe of the nanometer scale structure of materials in thin film and multilayered form. It has contributed especially to our understanding of soft condensed matter of interest in polymer science, organic chemistry, and biology and of magnetic hard condensed matter systems. In this paper we examine a number of key factors which have emerged that can limit the sensitivity of neutron reflection as such a probe. Among these is loss of phase information, and we discuss how knowledge about material surrounding a film of interest can be applied to help resolve the problem. In this context we also consider what role the quantum phenomenon of interaction-free measurement might play in enhancing the statistical efficiency for obtaining reflectivity or transmission data. [doi:[10.1063/1.3661979](https://doi.org/10.1063/1.3661979)]

I. INTRODUCTION

Over the past 25 years or so, specular neutron reflectometry (NR) has become established as a valuable probe for determining the nanometer scale structures lying beneath the exterior surfaces of hard and soft condensed matter thin films of interest in physics, chemistry, and biology.¹⁻⁴ As is well-known, neutrons are especially sensitive to hydrogen and atomic magnetic moments, thereby potentially complementing subsurface structural information that can be obtained from x-ray reflectivity measurements. More specifically, the scattering length density (SLD) depth profile along the surface normal, averaged over in plane, can be deduced from specular neutron reflectivity measurements (wavevector transfer Q normal to the surface). Under nearly ideal conditions, neutron reflectivities as low as 10^{-8} out to a Q of 0.7 \AA^{-1} from a lipid bilayer membrane have been measured with a corresponding spatial resolution in the SLD profile of half a nanometer.⁵ The SLD profile, in turn, is directly related to the corresponding material composition distribution—and if polarized neutron beams are employed, the vectorial magnetization depth profile of magnetic materials can be obtained as well.

Moreover, in specular neutron reflectometry, the phase can be determined exactly using reference structures, thereby enabling a first-principles inversion, and thus ensuring a unique result for the SLD profile.⁶ The ability to establish an unambiguous correspondence between reflectivity data and SLD profile is arguably the most important factor in making an accurate structure determination. When phase-sensitive methods are employed, what ultimately limits the accuracy

and spatial resolution of the SLD depth profile are the maximum attainable range of wavevector transfer Q and the statistical uncertainties in the measured reflected intensities.⁷ Clearly, by providing higher incident beam fluxes, the construction of advanced neutron sources can help expand the measurement envelope for specular neutron reflectometry, as can advances in beam optics (e.g., higher-efficiency polarizing supermirrors or the development of polychromatic beam instruments at steady state sources). So too, minimizing the amount of extraneous incoherent background scattering from the film substrate and other surrounding material increases the achievable signal-to-noise ratio. Moreover, since the interfacial roughness within the film itself, or of the supporting substrate, contributes to a fall-off of the reflection signal as well, efforts to reduce such roughness can also be of significant benefit. In the first part of this paper, Secs. II through V, we briefly review the current state of progress, regarding some of the issues identified above, in applying specular neutron reflectometry to structural investigations of thin film systems and give, as illustration, a recent example of a phase-sensitive NR study of an organic photovoltaic film system.

Although the success of conventional quantum mechanical theory in describing specular neutron reflection is remarkable, in ideal circumstances achieving a quantitative accuracy of the order of a few percent, this does not necessarily mean that the present understanding of the theory or its formulation is complete. In the second part of this article, we consider aspects of quantum theory which have not yet been routinely applied to reflection or transmission measurements of materials. We focus on other features of the quantum measurement process itself. In particular, a possible alternative approach to performing neutron reflectivity measurements, which involves the quantum phenomenon of “interaction-free measurement” (IFM), of the type first proposed by Renninger,⁸ Dicke,⁹ Elitzur and Vaidman,¹⁰ and realized in rudimentary fashion by Kwiat *et al.* with visible

^{a)}This paper is based on a presentation delivered at the symposium organized to acknowledge the scientific contributions of Professor Sunil Sinha, in conjunction with the SXNS-11 Conference held in Evanston, IL, in July of 2010.

^{b)}Electronic mail: charles.majkrzak@nist.gov.

light,¹¹ is critically examined. The scheme utilized by Kwiat *et al.* optimizes the efficiency for performing an IFM of the reflectivity (or transmission) by application of the quantum Zeno effect (which requires polarized photons or neutrons in their particular scheme). We examine whether an IFM scheme can lead to a statistically more efficient measurement of neutron reflectivity.

II. PHASE DETERMINATION AND DIRECT INVERSION

A. General description

It is well-known that diffraction measurements in general are subject to an intrinsic ambiguity due to the loss of phase information which results from measuring a reflected wave intensity from a single pattern or reflectivity curve as opposed to being able to directly measure the reflection amplitude which contains the phase explicitly. In neutron or x-ray crystalline powder diffraction over the range of Q normally covered, the interaction typically is sufficiently weak that the diffraction can be described accurately within the Born approximation or kinematical analysis in which a Fourier transform connects the reflection amplitude and SLD distribution. Here, the periodic nature of the scattering object helps make it possible to retrieve phase information.¹² Alternatively, controlled isomorphic substitution of one or more atomic constituents of the crystallographic unit cell can lead to multiple diffraction data sets which can then be simultaneously analyzed to extract the phase.

Similarly, in specular NR nonunique solutions arising from loss of phase information are problematical if reliable complementary information is unavailable to resolve such ambiguities (see, for instance, Refs. 13 and 14 for further discussion and illustrative examples). However, for NR the possibility of a non-periodic SLD profile in combination with the necessity of properly accounting for refractive effects in the solution of the wave equation (at sufficiently low Q in the vicinity of the critical angle for mirror reflection) requires a somewhat different approach in dealing with the phase problem.

As it turns out, the specular neutron reflection process (restricting the present discussion to unpolarized neutrons and nonmagnetic materials) can be described accurately by solving the one-dimensional Schroedinger wave equation exactly (which is possible to do piece-wise continuously for any arbitrarily shaped SLD profile). The exact solution of the Schroedinger equation can be formulated in terms of a set of linear algebraic equations relating the reflection and transmission amplitudes and characterized by a “transfer” matrix containing all the information about the SLD distribution. For typical neutron reflection studies of the nanometer scale structure of thin film layered materials, the nuclear interaction potential can be effectively described in terms of a refractive index or scattering length density (SLD). If the SLD is real, with no appreciable imaginary component associated with an absorptive process (typically the case for most isotopes), then it can be shown that there is a one-to-one correspondence between the complex reflection amplitude, measured as a function of wavevector transfer Q , and the SLD depth profile that gives rise to it (see, for example, Refs. 15, 16, and 7) (it

is further assumed that the effects of any possible bound states are negligible). In other words, this isomorphism ensures a unique relationship between the reflection amplitude and SLD. Consequently, both the direct scattering problem, i.e., calculating the reflection amplitude from a given SLD depth profile, and the inverse problem, i.e., deducing the SLD profile from a specific reflection amplitude curve, are solvable from a first-principles calculation involving the one-dimensional Schroedinger equation. For infinite data sets with no uncertainty, the relationship between reflection amplitude curve and SLD profile thus is unambiguous. The details of this mathematical connection were worked out in the mid 20th century by Gel’fand, Levitan, and Marchenko (GLM) and others¹⁵ and involve the solution of an integral equation — or, alternatively, a partial differential equation, as developed more recently by Sacks.^{16,17}

It was subsequently discovered that the reflection amplitude containing the phase that was needed to perform the GLM inversion could be recovered from measurements on multiple composite thin film systems, each consisting of the common film of interest, the SLD profile of which was unknown, and a different adjacent reference layer SLD profile or surrounding medium.^{18–23} The transfer matrix naturally separates into a product of two matrices, one corresponding to the film of interest and the other to the adjacent known reference. Although direct inversion is possible once the complex reflection amplitude has been determined, it is also possible to extract the unique SLD profile of the unknown film by simultaneous fitting of the composite system reflectivity data sets themselves,²⁴ but this process is less direct.

Because true inversion may not be strictly possible in the presence of appreciable absorption, direct phase-inversion methods are more limited for x-ray applications. Nonetheless, significant phase information can be retrieved if the substrate SLD is tuned by varying the x-ray wavelength through its absorption edge.²⁵ Leeb *et al.* have investigated other methods for dealing with absorptive materials.²⁶

In summary, for specular neutron reflection, the complex reflection amplitude or phase associated with an “unknown” segment of a composite film structure can be determined exactly, using reference segments, and a subsequent, first-principles inversion can be performed, thereby ensuring a unique result (some examples are given in Refs. 27 and 28). Thus, the phase-sensitive neutron reflection/inversion process results in a real-space picture without fitting or any adjustable parameters. However, as will be shown in following sections, there are other important advantages associated with the phase-inversion process.

B. Rigorous uncertainty analysis

The accuracy and spatial resolution of the SLD depth profile retrieved through phase-sensitive reflectivity measurements and direct inversion are ultimately limited by the maximum Q attainable and the statistical uncertainty in the measured reflected intensities. The fact that there exists a one-to-one correspondence between the reflection amplitude spanning all Q and the SLD profile responsible for it also makes it possible to perform a mathematically rigorous

analysis of the effect of these uncertainties on the SLD profile that is deduced from phase-sensitive neutron reflectivity data. Figure 1 shows two model composite system reflectivity data sets for a common Cr/Au/h-lipid/d-lipid membrane system adjacent to each of two different substrate media (Si and Al₂O₃) that serve as references. The reflectivities in each of the two data sets include a certain amount of statistical error and both sets are truncated at the same maximum value of Q . The consequences of the statistical uncertainty in and truncation of these two reflectivity data sets — as computed according to the formalism developed in Ref. 7 — are shown in Figs. 2 and 3, respectively. Since it is far beyond the scope of this review to do justice to the power of this statistical analysis of phase-inversion specular NR, the interested reader is directed to the original paper for a comprehensive treatment.

It is perhaps worth noting here that a gain of a factor of two in the spatial resolution in the SLD profile is obtained by performing phase-sensitive NR measurements as opposed to what is possible with a single, phaseless NR data set truncated at the same maximum value of Q .⁶

C. Diagnostic for in-plane homogeneity

It has also been found that the imaginary part of the complex reflection amplitude, which is recovered in the phase-sensitive measurement process, contains valuable information about in-plane variations of the SLD on a length scale comparable to the dimensions of the projected area of the neutron wave packet.²⁹ The size of the areas of different SLD in plane relative to the effective neutron wave packet coherence length can have significant impact on the analysis of the reflected intensity. If the coherence length is large compared to the dimensions of in-plane regions of different SLD, then those variations are effectively averaged over in-

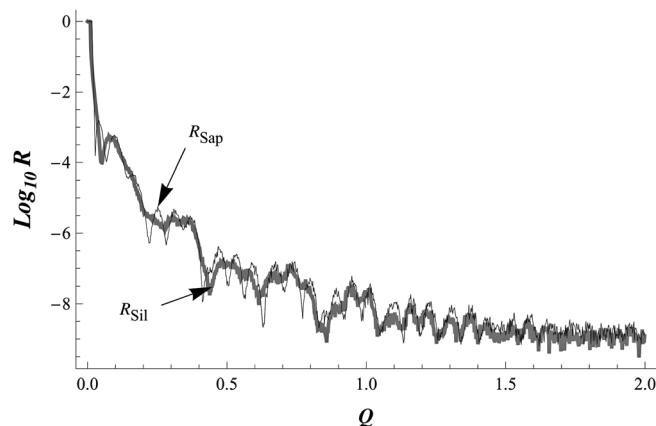


FIG. 1. Two composite system model reflectivity data sets for a common Cr/Au/h-lipid/d-lipid membrane system on each of two different surrounding media (Si and Al₂O₃) that serve as references. The reflectivities in each of the two data sets include a certain amount of statistical error and both sets are truncated at the same maximum value of Q (the scale is in inverse Angstroms). The resultant effects on the SLD profile as a consequence of the statistical uncertainty in the reflected intensities and truncated range of Q are shown in Figs. 2 and 3, respectively — as computed directly according to the formalism developed in reference 7 that is enabled by the isomorphism between reflection amplitude and SLD profile (as discussed in the text). [Reprinted from N. F. Berk and C. F. Majkrzak, *Langmuir* **25**, 4132 (2009), Fig. 2.]

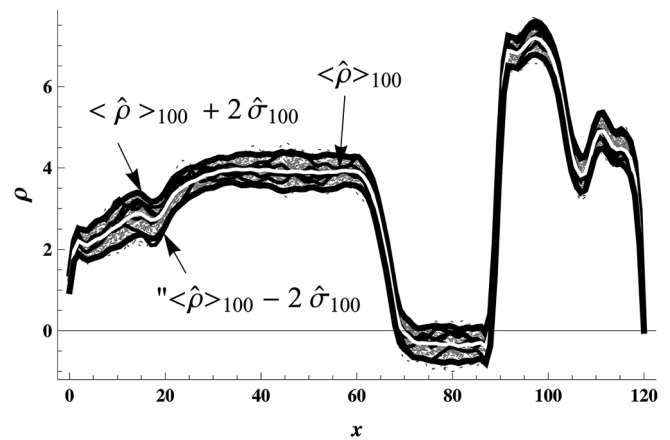


FIG. 2. SLD profile for a film system consisting of, from left to right, a relatively thin Cr layer, an approximately 50 Å thick layer of Au, a protonated alkane thiol layer, and a deuterated lipid layer adjacent to an aqueous reservoir (the substrate, either Si or Al₂O₃, is located on the left, below $x=0$). The effective spread of SLD values was generated by calculations for 100 model sample systems, assuming an incident intensity of 10^4 up to a maximum Q of 2.0 inverse Angstroms. The central white line represents the average SLD for the 100 model sample systems, $\langle \hat{\rho} \rangle_{100}$, whereas the outer dark lines indicate \pm two estimated standard deviations. The units of the abscissa and ordinate are Å and 10^{-6} Å⁻², respectively. See Ref. 7 for a detailed discussion of the computations. [Reprinted from N. F. Berk and C. F. Majkrzak, *Langmuir* **25**, 4132 (2009), Fig. 4.]

plane insofar as the specular reflectivity is concerned. On the other hand, if the converse is true and each neutron wave packet interacts with only a single region of one particular scattering length density, then the net measured reflected intensity will represent an already weighted, incoherent sum of the reflected intensities from each different type of area. Not knowing this information can potentially cause a misinterpretation of the reflectivity data and result in an erroneous analysis.

As it happens, the imaginary part of the reflection amplitude has two symmetric roots associated with the solution of a quadratic equation. Although only one of these roots has

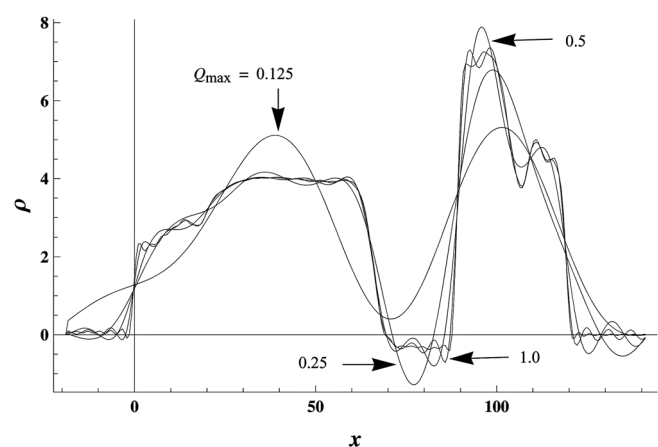


FIG. 3. Here are shown the effects of truncating the reflectivity data at various values of maximum Q alone — i.e., without the degradation associated with counting statistics. The units of the abscissa and ordinate are Å and 10^{-6} Å⁻², respectively. Once again, see reference 7 for a detailed discussion of the computations involved which are enabled by the mathematical isomorphism between SLD and complex reflection amplitude. [Reprinted from N. F. Berk and C. F. Majkrzak, *Langmuir* **25**, 4132 (2009), Fig. 10.]

physical meaning, and is straightforwardly identified, plotting the two roots simultaneously reveals a symmetric pair of oscillatory functions of Q which have coincident zero-crossing points at predictable values of Q .²⁹ If the imaginary part of the reflection amplitude, $\text{Im } r$, as obtained from a phase-sensitive specular neutron reflectivity measurement, displays gaps between roots where zeros ought to occur, this indicates the presence of inhomogeneous regions of different SLD in plane that are of sufficient area as to make averaging by the neutron wave packet impossible. Figure 4 shows several sets of $\text{Im } r$ obtained on films of a nominally similar system, a supposed monolayer of alkane thiol on a Au layer deposited on a Si substrate, but for different conditions of an adjacent aqueous reservoir — namely, with and without the presence of various concentrations and sizes of air bubbles.³⁰ For a comprehensive analysis of this diagnostic tool, refer to Ref. 29.

III. ROLE OF INTERFACIAL ROUGHNESS

It is, of course, important to deposit the film system of interest on a sufficiently flat substrate support so as not to degrade the instrumental Q resolution. On the other hand, the interfacial roughness on a more local length scale can have a significant direct effect on the spatial resolution in the SLD depth profile. Moreover, the magnitude of the reflected signal for a rough film falls off even more quickly than the $1/Q^4$ behavior for a perfectly sharp interface, potentially limiting the maximum Q value attainable in an actual experiment — and thereby indirectly limiting the spatial resolution. Figure 5 shows a SLD profile for alpha-hemolysin embedded in a lipid bilayer along with an illustration in real space of the corresponding molecular structure.³¹ Model SLD depth profiles for this system at various concentrations of the alpha-hemolysin integral membrane protein are plotted in Fig. 6. Figures 7 and 8 show the corresponding model reflectivity data for the different coverages of the protein without

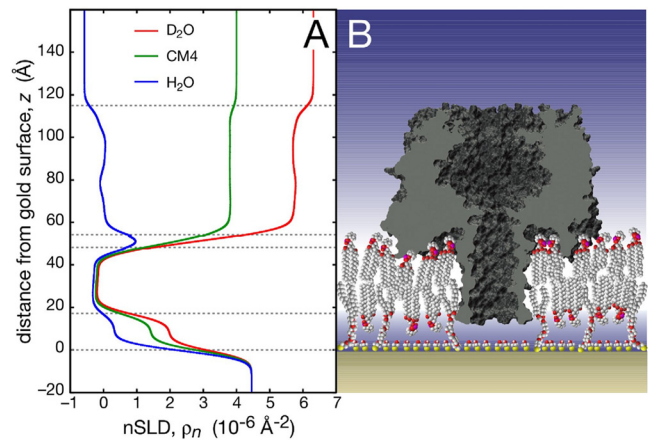


FIG. 5. (Color online) SLD profile for alpha hemolysin embedded in a lipid bilayer along with an illustration in real space of the corresponding molecular structure.³¹

and with a given amount of interfacial roughness, respectively. Clearly the degree of roughness can be a major factor in achieving a desired spatial resolution in specular reflectometry studies.

IV. ILLUSTRATIVE EXAMPLE: PHOTOVOLTAIC FILM

As an illustration of the sensitivity of NR for probing current scientific and technical problems involving the nanostructure of thin film materials, consider the following example from the ongoing development of organic photovoltaic thin film devices. In particular, a system composed of a 1:1 by weight blend of [6,6]-phenyl-C61-butyric acid methyl ester (PCBM) nanoparticles and poly(3-hexylthiophene) (P3HT) has recently been studied.^{32,33} NR is especially well-suited to probe the morphology of these films because of the large degree of scattering contrast possible between the two organic components of the film system. Polymer-based solar cell performance is largely determined by nanoscale structures

Three differently prepared HBMs

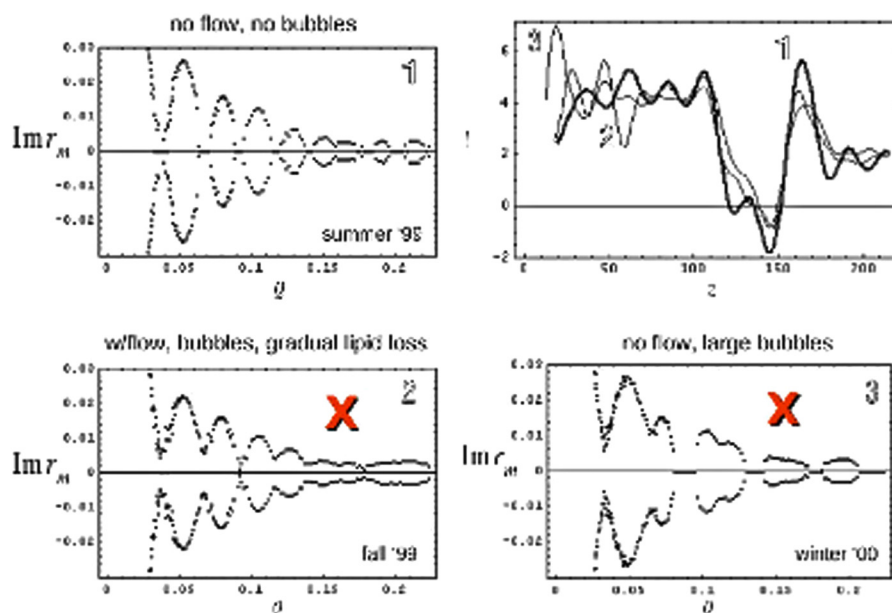


FIG. 4. (Color online) Several different plots $\text{Im } r(Q)$ vs Q for an alkane thiol, hybrid bilayer membrane (HBM) on a Au layer deposited on a Si substrate adjacent to an aqueous reservoir under different conditions of flow and bubble formation. Also shown is a plot in the upper right hand corner of the corresponding SLD profiles.³⁰ Only data set number 1 appears sufficiently homogeneous in the plane of the film on a length scale over which the neutron wave packet effectively averages, according to the criterion based on the zeros of $\text{Im } r(Q)$ (“X” indicates an inhomogeneous case). The dimensions of Q in the horizontal scale for the plots of $\text{Im } r(Q)$ are inverse Angstroms whereas the units for z in the plot of the SLD are Angstroms. The vertical axis in the SLD plot is in units of 10^{-6} \AA^{-2} . The incoherent reflection associated with samples 2 and 3 introduces significant artifacts in the SLD profile beyond what is caused by statistical uncertainty in and truncation of the reflectivity data.

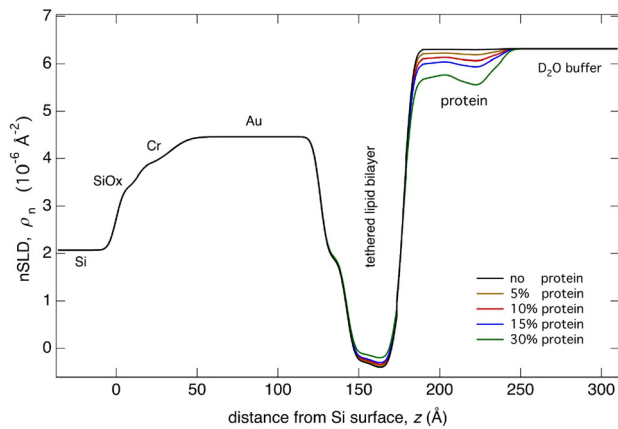


FIG. 6. (Color online) Variations in a model SLD profile for a selection of different concentrations of the protein. Interfacial roughnesses are included: 21.6 Å FWHM for the Cr/Au and 8.752 Å FWHM for each of the other interfaces.

because the active layer exhibits relatively short exciton diffusion lengths. This comes about because of the sufficiently large Coulombic attraction between the photogenerated exciton (bound electron-hole pair) which requires an interface to promote dissociation. In addition, the large Coulombic attraction and inherent electrical properties of P3HT limit the exciton diffusion length to approximately 5 to 10 nm prior to recombination. The duality of length scales, i.e., roughly a 200 nm thickness requirement to accommodate typical photon absorption of conducting polymers (the conducting polymer generates the exciton upon absorption of light) and the 10 nm exciton diffusion length (the exciton subsequently migrates to the nanoparticle where dissociation occurs at the interface), dictates that a comb-like structure would be ideal, although other related, but more practically fabricated morphologies have been suggested. It is crucial to understand what structure actually results from a given fabrication process. Other techniques, such as transmission electron microscopy (TEM), can be insensitive to the morphology due to a lack of intrinsic contrast between the film components. In this case NR measurements can be decisive.

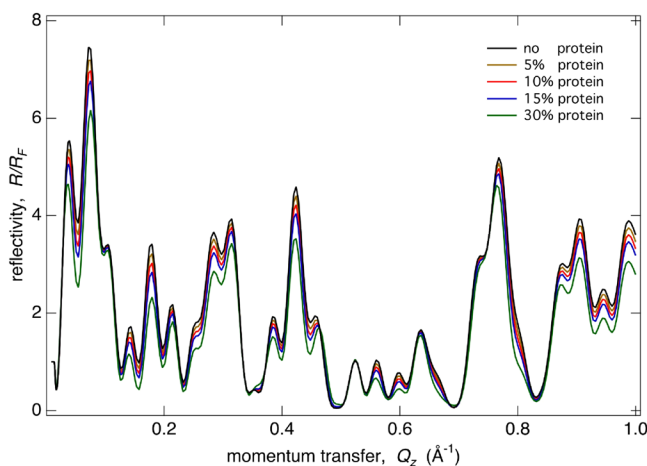


FIG. 7. (Color online) Corresponding model reflectivity data for the different coverages of the protein shown in the SLD profile of Fig. 6 but *without* interfacial roughness.

A phase-sensitive measurement was carried out recently on the specific organic photovoltaic film system mentioned above.^{32,33} Figure 9 shows two composite reflectivity data sets, one corresponding to the photovoltaic film in air, the other with the same film adjacent to (and in direct contact with) a reservoir of D₂O (the air and D₂O reservoir serve as the two references required to obtain the phase information associated with the photovoltaic film).

Also shown in Fig. 9 along with the composite system reflectivity data sets are simultaneous fits. The data sets were also directly analyzed to yield the real and imaginary parts of the complex reflection amplitude corresponding to the photovoltaic film alone whose SLD depth profile is being sought. Figure 10 shows the real part of the reflection amplitude, $\text{Re } r(Q)$, which was obtained from the composite reflectivity data sets directly, without fitting or use of any adjustable parameters.

In Fig. 11 are shown two SLD depth profiles for the photovoltaic film as obtained from the composite system NR data sets: one obtained from a simultaneous fit of the two data sets; and the other resulting from a direct, first-principles inversion of the $\text{Re } r(Q)$ curve of Fig. 10. The two results are in good agreement, within the degree of uncertainty allowed by the statistical error in the reflectivity data and the truncation at the maximum value of wavevector transfer Q . This degree of consistency is remarkable and indicative of the inherent importance of the phase in identifying the unique, physical SLD profile associated with the NR data.

Once again, the differences that do remain between the SLD profile obtained by direct inversion and that deduced by phase-sensitive simultaneous fits are indicative of the degree of uncertainty in the NR data associated with statistical variation and truncation, as discussed above in the preceding section. The resultant SLD profile for this particular sample indicates a concentration of the PCBM nanoparticles at the substrate as well as at the air interface. A possible PCBM-P3HT morphology corresponding to this SLD profile is rendered in the inset of Fig. 11.

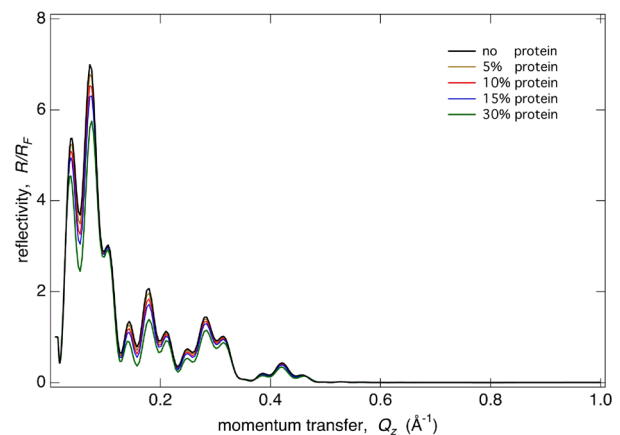


FIG. 8. (Color online) Corresponding model reflectivity data for the different coverages of the protein shown in the SLD profile of Fig. 6 with interfacial roughness included: 21.6 Å FWHM for Cr/Au and 8.752 Å FWHM for each of the other interfaces. The interfacial roughness markedly reduces the reflectivity signal at higher values of Q .

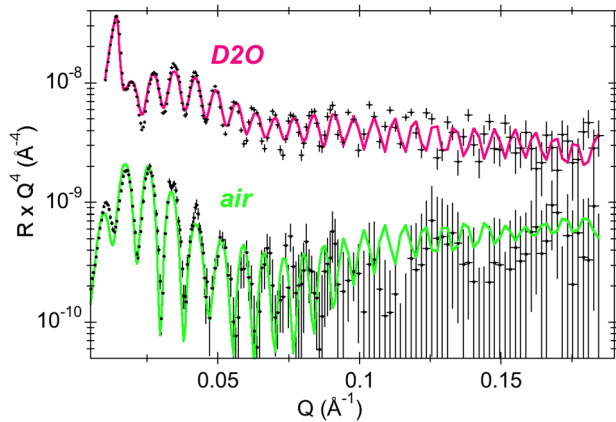


FIG. 9. (Color online) Two composite reflectivity data sets, one corresponding to the photovoltaic film in air, the other with the same film adjacent to (and in direct contact with) a reservoir of D_2O (the air and D_2O reservoir serve as the two references required to obtain the phase information associated with the photovoltaic film).^{32,33} [Reprinted from J. W. Kiel, M. E. Mackay, B. J. Kirby, B. B. Maranville, and C. F. Majkrzak, *J. Chem. Phys.* **133**, 074902-1 (2010), Fig. 4(a).]

If sufficient in-plane inhomogeneity is present in the film, a question can be raised about whether its length scale is such as to lead to a misinterpretation of the specular data as discussed in Sec. II C. Figure 12 shows a plot of $\text{Im } r(Q)$ versus Q for another of the photovoltaic films examined in this study which displays well-defined zeros that are indicative of effective averaging of the neutron wave packet, as discussed earlier [$\text{Im } r(Q)$ for the film whose $\text{Re } r(Q)$ is shown in Fig. 10 is essentially of equivalent quality]. Thus, in this regard, the SLD profile deduced is representative of a single, in-plane average.

Another issue is the appearance of artifacts in the structure of the SLD profile arising from the truncation of the reflectivity data, as indicated above in Fig. 3 of Sec. II B. This is a particular concern at the edges of a rectangular profile — in analogy with truncation of a Fourier series representation of a rectangle which results in the appearance of

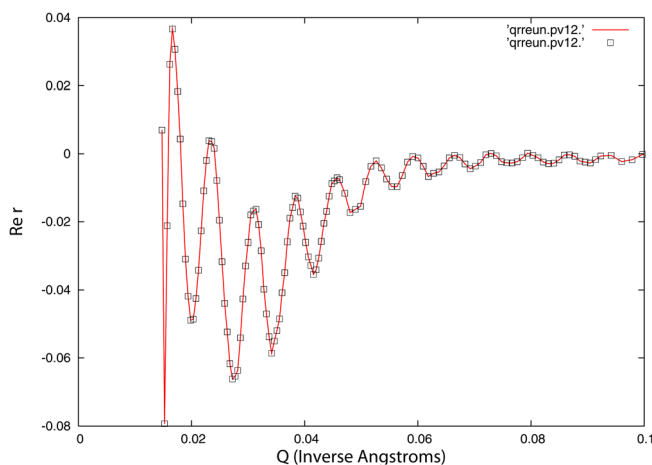


FIG. 10. (Color online) Real part of the reflection amplitude, $\text{Re } r(Q)$, which was obtained from the composite reflectivity data sets directly, without fitting or use of any adjustable parameters. [Reprinted from J. W. Kiel, M. E. Mackay, B. J. Kirby, B. B. Maranville, and C. F. Majkrzak, *J. Chem. Phys.* **133**, 074902-1 (2010), Fig. 4(b).]

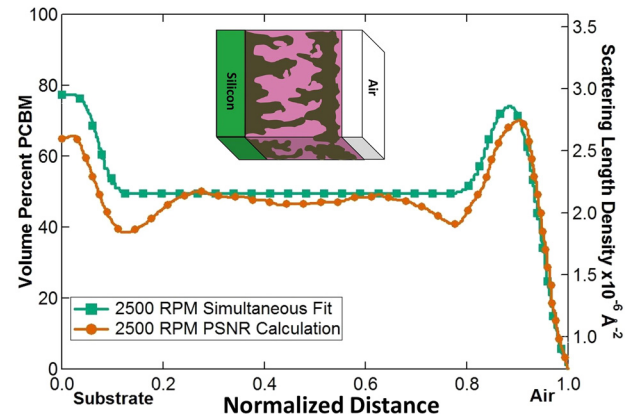


FIG. 11. (Color online) Two SLD depth profiles for the photovoltaic film as obtained from the composite system NR data sets: one obtained from a simultaneous fit of the two data sets; and the other resulting from a direct, first-principles inversion of the $\text{Re } r(Q)$ curve of Fig. 10. The two results are in good agreement within the degree of uncertainty allowed by the statistical error in the reflectivity data and the truncation at the maximum value of wavevector transfer Q . [Reprinted from J. W. Kiel, M. E. Mackay, B. J. Kirby, B. B. Maranville, and C. F. Majkrzak, *J. Chem. Phys.* **133**, 074902-1 (2010), Fig. 4(c).]

additional structure at the edges commonly known as the Gibbs phenomenon. To investigate the possibility of such an artifact being misinterpreted as a concentration of SLD at the interfaces of the photovoltaic film, model calculations were performed using the phase-inversion formalism [i.e., inverting a model $\text{Re } r(Q)$ to obtain the corresponding unique SLD profile], as a function of maximum Q . The SLD profiles obtained by inversion from model data sets — which were in turn generated from corresponding SLD profiles, one for a strictly rectangular shape and another close to that obtained experimentally for the actual photovoltaic film — are depicted in Fig. 13. For each of the two model SLD profiles in Fig. 13, there corresponds two profiles, one obtained from inversion of $\text{Re } r(Q)$ for Q up to a maximum of 0.1 inverse angstroms and the other for a maximum Q of 0.4. In either case, the artifacts in SLD introduced by a finite cutoff of the

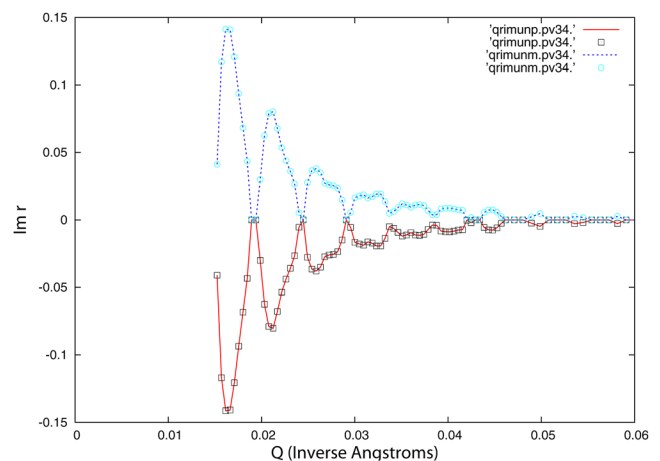


FIG. 12. (Color online) Plot of $\text{Im } r(Q)$ vs Q for another of the photovoltaic films examined in this study which displays well-defined zeros that are indicative of effective averaging of the neutron wave packet. [Reprinted from J. W. Kiel, M. E. Mackay, B. J. Kirby, B. B. Maranville, and C. F. Majkrzak, *J. Chem. Phys.* **133**, 074902-1 (2010), Fig. 6.]

reflectivity data are negligible in comparison to the peaks in SLD associated with a buildup of actual material at the interfaces. This provides further confidence that the SLD deduced from the phase-sensitive NR measurements performed on the photovoltaic film are physically meaningful.

The rather large PCBM concentration at the solid substrate is undesirable because holes would be typically conducted through it. It would be more advantageous to have an inverted concentration profile with a larger PCBM concentration at the air interface since it is an electron transporter. The details of this study, including the implications of the results on future development of organic photovoltaic films can be found in references.^{32,33} What is clear is that NR has a valuable role to play in determining the morphology of such films produced by various fabrication processes.

V. INTERACTION-FREE MEASUREMENT

It is remarkable that specular neutron reflectometry measurements can be so accurately described by the one-dimensional Schrodinger wave equation, for both the “forward” and “inverse” scattering problems, as discussed in the previous sections of this paper. In describing the phase-sensitive NR measurements, it was shown how surrounding the sample object film with reference materials makes it possible to obtain more than simply the reflected intensity from the object. In some sense we effectively modified the object in a controlled and predetermined way so as to enable the extraction of crucial phase information corresponding to the original object. What if we were to go yet a step further and immerse the object of interest in something more than just surrounding reference material, say in an interferometer — would it then be possible to retrieve equivalent information in a statistically more efficient manner? As alluded to in the Introduction and discussed specifically in this section, the quantum phenomenon of “interaction free measurement” (IFM) may offer one possible way of addressing such questions.

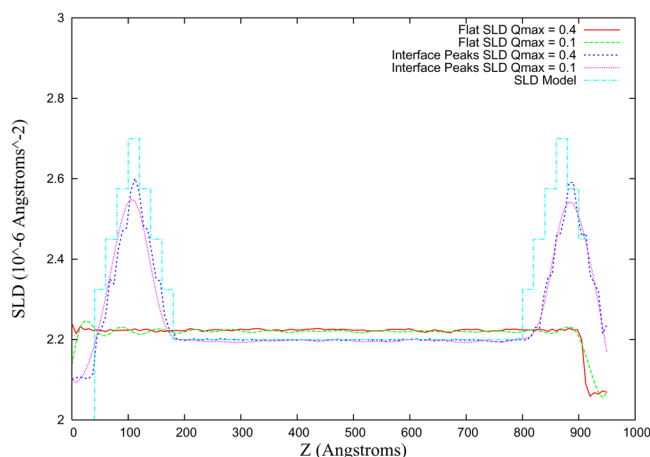


FIG. 13. (Color online) SLD profiles obtained by inversion from model data sets — which were in turn generated from corresponding SLD profiles, one for a strictly rectangular shape and another close to that obtained experimentally for the actual photovoltaic film. See text for detailed discussion. [Reprinted from J. W. Kiel, M. E. Mackay, B. J. Kirby, B. B. Maranville, and C. F. Majkrzak, *J. Chem. Phys.* **133**, 074902-1 (2010), Fig. 7(a).]

A. Introduction to interaction-free measurement

The idea of “interaction-free” measurement was introduced decades ago by Renninger,⁸ Dicke,⁹ Elitzur and Vaidman¹⁰ and realized in rudimentary fashion by Kwiat *et al.* with visible light.¹¹ In the time since there has been a resurgence of interest in this phenomenon and additional papers on the subject have been published. A good review of the fundamental concepts and their implications, which also includes experimental demonstrations, has been written by Kwiat.³⁴ The *Scientific American* article by Kwiat *et al.*³⁵ is also an excellent semi-quantitative exposition of the essential idea. The term “interaction-free” measurement is in a sense a misnomer, however, and some objection has been raised regarding this usage. As we will see in the discussion below, within an interferometer in which an opaque object blocks one of two possible paths, a nonabsorbed photon or neutron can only have traveled the path without the object. This does not imply the absence of a coupling term in the Hamiltonian describing the system as a whole.³⁴ What the term IFM actually refers to is a situation wherein we learn something about an object, e.g., its transmittivity, within a device such as an interferometer from a probe, e.g., either a photon or a neutron, which was not absorbed by the object. It has been shown, both theoretically and experimentally^{11,36,37} that the efficiency for detecting the presence of an opaque object within an interferometer can be greater than 50% (approaching unity under ideal conditions) if another quantum phenomenon, the quantum Zeno effect, is applied within the interferometer. The IFM idea has even recently been explored for application to electron microscopy.³⁸ Although much of the earlier published work on IFM focused on opaque objects, the efficiency for measurements of semitransparent objects (of much more general interest) have been considered more recently.^{39–41} We present here calculations that also deal with semitransparent objects, but for the case of neutrons rather than light and with a specific interest in determining what the corresponding efficiency would be for measuring any value of the transmission (or equivalently the reflectivity), between 0 and 1, at a given accuracy compared to that for a conventional measurement. Although we consider transmission measurements, there is essentially no difference in treating a specular reflection process (in which neutrons are lost by elastic scattering rather than absorption).

B. Interaction-free measurement of an opaque object with a Mach-Zehnder interferometer

To begin our discussion, consider first the specific IFM example presented by Kwiat *et al.*^{11,35} involving a “thought” experiment with a Mach-Zehnder interferometer like that depicted in Fig. 14. The splitting element divides a single incident photon wavefunction into two equal parts, one of which propagates along the upper route while the other follows the lower path. Upon coming together at the combining element, interference between the two waves occurs, the result of which is recorded in two detectors. The path lengths and composition of the combining element have been chosen so that one of the detectors, designated the “light” detector,

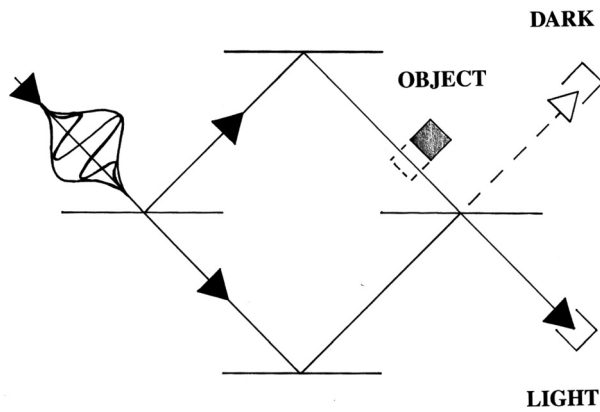


FIG. 14. Mach-Zehnder type interferometer constructed of partially reflecting films (indicated by the black horizontal bars). A neutron wavepacket incident from the upper left is partially reflected and transmitted by the first film or “splitter”. Again, considering the passage of a single neutron at a time through the entire apparatus, there are two possible paths, upper and lower. Upon reaching the last film element on the right, “partial” waves from the two paths interfere and recombine via a coherent interaction between the neutron wavefunctions and the material potential of the film. As a result of the recombination, there are probabilities for detecting the neutron at the end of either the upward or downward paths. Note that the shape of the neutron wavepacket, as characterized by its longitudinal and lateral coherence lengths, parallel and perpendicular to its mean wavevector, respectively, determines how the neutron interacts with the interferometer. The path lengths and composition of the combining element have been chosen so that one of the detectors, designated the “light” detector, records complete constructive interference whereas the other “dark” detector registers only total destructive interference (no photon). This set-up is analogous to the double-slit apparatus, with the “light” and “dark” detectors corresponding to positions on the screen displaying the diffraction pattern where light and dark bands are observed, respectively. When a light absorbing object is placed in the upper path of the interferometer, the interference cannot occur. Instead, the probability of a given photon being absorbed by the object in the upper path is 50%. There is also a 50% probability that a photon will reach the combiner via the lower path.

records complete constructive interference whereas the other “dark” detector registers only total destructive interference (no photon). This setup is analogous to the double-slit apparatus, with the “light” and “dark” detectors corresponding to positions on the screen displaying the diffraction pattern where light and dark bands are observed, respectively.

When a totally light-absorbing object is placed in the upper path of the interferometer, the interference cannot occur. Instead, the probability of a given photon being absorbed by the object in the upper path is 50%. There is also a 50% probability that a photon will reach the combiner via the lower path. However, with no other wave present to interfere with, it now has an equal chance of reaching either the “light” or “dark” detector. (A fraction of a photon cannot be absorbed by the object or registered in one of the detectors.) If the photon registers in the “light” detector, we do not learn whether or not an object is blocking the upper path — but if the photon is registered in the “dark” detector, then we know immediately and with certainty that the upper path must be blocked. And this is accomplished with a photon that has not interacted with the object in any conventional sense (no exchange of momentum or energy and without absorption). It is emphasized in reference ³⁵ that this detection process, while it works only some of the time (50% efficiency), when it does work, it works completely. An actual experiment is

then described which was performed to verify that this really happens.^{11,35}

In order to improve the efficiency for this IFM process, the application of another quantum phenomenon, the so-called quantum Zeno effect, within an interferometer was proposed.¹¹ One manifestation of the quantum Zeno effect uses a series of successive pairs of polarization rotators and projection devices (polarizing material which selects out either the horizontal or vertical component of the polarization vector for photons or spin “+” or “−” in the case of neutrons) that make it possible to inhibit the rotation of a photon’s or neutron’s polarization vector. This device can then be used in conjunction with an interferometer to increase the efficiency of the process for detecting a blocking object with photons that never “see” it.¹¹ In effect, the Zeno phenomenon creates a means of regulating the probability amplitude of the photon along the interferometer path containing the object, so as to affect the efficiency of the IFM. In the following sections we will consider the IFM process for the more general case of a semitransparent object, which in principle applies to typical transmission or reflectivity measurements performed on material objects, including the types of thin film systems of primary interest in this paper.

C. Interaction-free measurement of a semi-transparent object with a Michelson interferometer

Consider now measuring the transmission of a semi-transparent object via an interaction-free scheme that employs a modified Michelson interferometer in which the quantum Zeno effect can be applied. The principal goal is to calculate the uncertainty in the measurement of the transmission function obtained in this way so that it can be compared to that for a simple, conventional measurement of the transmission. We will examine the case for polarized neutrons here, in contrast to that for optical wavelength photons which were used in Ref. 11 and other related papers on the subject. To start, consider the schematic of the modified Michelson interferometer depicted in Fig. 15.

One of the features which makes this Michelson interferometer slightly modified is the use of a pair of orthogonal reflecting mirrors instead of the conventional single flat pieces. The reason for doing this is to ensure that the reflected neutron wave cannot travel back from where it came and thereby allow the possibility of a standing wave state between successive mirror elements. Another means to accomplish this in the conventional Michelson configuration would be to incline opposing mirrors at the ends of the interferometer a relatively small degree away from parallel alignment. However, for our present purpose, doing so would cause progressive displacement of the trajectories relative to the reflecting elements for multiple circuits or loops within the interferometer. Note also, as mentioned in the caption of Fig. 15, the translational separation of spin “+” and “−” paths below the splitter is not real but depicted as such only for clarity of presentation — in fact, the two spin state paths overlap exactly so that recombination of components can occur at the splitter.

Suppose a single neutron enters the interferometer from the bottom through the “gate” mirror which can be opened to

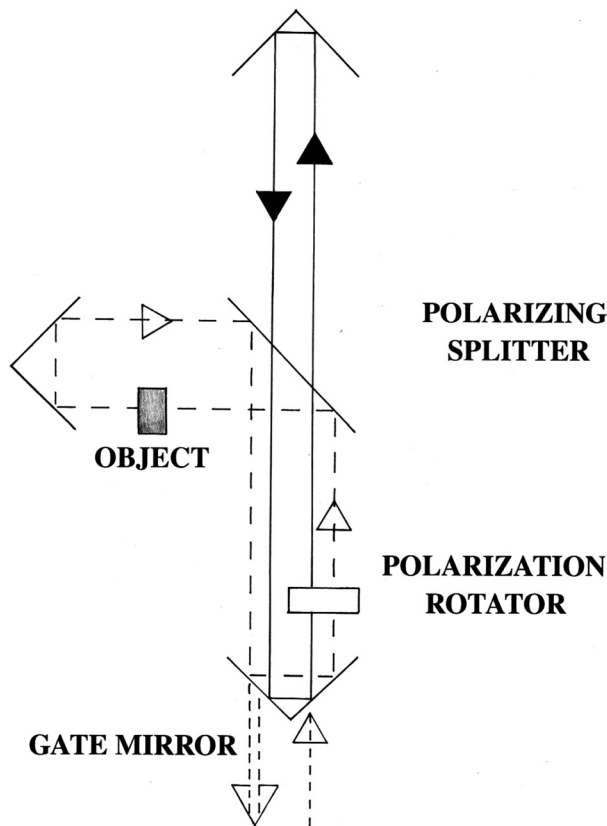


FIG. 15. Modified (slightly) Michelson interferometer as described in detail in the text. Above and to the left, the neutron is in one or the other pure spin eigenstate, “+” and “-”, respectively, (quantization axis defined by a magnetic “guide” field is along the z axis defined to be normal to the diagram) whereas below the polarizing beam splitter the neutron can be in a mixed or precessing polarization state. The separation of paths below the splitter is not real and is shown this way only for clarity. Note that the polarization component transmitted by the splitter never encounters the object.

allow entry and then, subsequently, closed to trap the neutron within the interferometer loop circuit. At some later time the gate mirror can be opened again to allow that neutron to escape, after one or more loops of the interferometer circuit, to be detected outside of the interferometer (if it had not been absorbed by the object in traversing the horizontal path segment). An alternative, but equivalent, geometry can be imagined where m successive stages, each stage or “unit cell” representing one cycle, are arranged in series. In this way of looking at it, the neutron enters one end, say from the left, and exits the other, on the right, without the need for a gate mirror. This view more explicitly separates space and time in visualizing the system to be described by the time-independent Schroedinger wave equation, i.e., in finding a “stationary state” solution for the propagation of a neutron through the interferometer m times. The Appendix offers a concise treatment for this linear geometry.

Let us follow the “trajectory” of this one neutron within the interferometer. We can describe the passage quantitatively by writing down the wave function for each segment between successive interferometer elements. For the time being, we will represent a single neutron as a plane wave, with wave vector k , which is a solution of the time-independent

Schroedinger equation of motion. Because we are dealing with polarized neutrons, the wave function must have the form of a two-component spinor, the evolution of which in time and space is described by a pair of coupled, linear, second order differential wave equations. Nonetheless, for the analysis of the propagation of the neutron through the interferometer described here, it suffices to treat the two spin states independently almost everywhere, each with a wave equation of identical form, since no “spin-flip” potentials are present within the apparatus except for the spin rotator device. However, for that part of the interferometer path passing through the spin rotator, we are required to treat transitions between spin states explicitly, which we will do.

Because the Schroedinger equation is linear, an appropriately weighted linear superposition of the stationary state plane wave solutions (each with a different k value) of the time-independent Schroedinger equation can be used, subsequently, to construct a wave packet solution of the time-dependent Schroedinger equation. In practical circumstances involving actual measurements with real interferometers, a wavepacket representation of the neutron ensures sufficient localization that the different possible “paths” through the interferometer are effectively distinct as are successive optical elements (e.g., mirrors) along a given path. On the other hand, the fact that a single plane wave is also a legitimate solution of the Schroedinger equation enables a great simplification of the mathematical analysis. That is, we need deal with only a single plane wave state knowing that the wave packet solution is composed of a simple linear superposition of plane wave states which are of identical form. Note that the representation of the neutron by a single plane wave in no way precludes the description of the division of the wave function by a splitting device or of its later recombination within the interferometer.

The general representation of the neutron for our present purposes is a plane wave function spinor consisting of two components corresponding to the pure “+” and “-” distinct “eigen” states relative to a quantization axis defined by a magnetic field along a particular direction in space. We have selected this magnetic “guide” field to be along the z axis which is normal to the plane of the interferometer schematic shown in Fig. 15. The wave function Ψ (a spinor) is written as

$$\psi = C_{0+} \exp(ik_+r) \begin{pmatrix} 1 \\ 0 \end{pmatrix} + C_{0-} \exp(ik_-r) \begin{pmatrix} 0 \\ 1 \end{pmatrix}. \quad (1)$$

Since we need only talk about the propagation of the wave along one straight section of path through the interferometer at any time, we will always take “ r ” to be a direct measure of distance along the direction of propagation of the neutron wave as defined by its wavevector k . If k_0 is the value of the neutron wavevector in vacuum and n_{+-} is the neutron refractive index, which is a measure of the strength of interaction between the neutron with matter (nuclear potential) and magnetic field, then $k_{+-} = n_{+-} k_0$. It is assumed that these interactions are at wavevector magnitudes sufficiently small that matter appears continuous. C_+ and C_- (as well as C_{0+} and C_{0-}) are, in general, complex numbers and represent the

probability amplitudes for the neutron being in the “+” or “−” spin states, respectively. $|C_+|^2$ and $|C_-|^2$ represent the respective probabilities of finding the neutron in the spin “+” or “−” state.

Assume that the neutron enters the interferometer circuit for the first time, through the momentarily open lower gate mirror, prepared to be in the pure “+” spin state so that $C_{0-} = 0$. The neutron wave next encounters the polarization rotator which consists of a relatively small region of space within which exists a uniform magnetic field which is orthogonal to the magnetic guide field that exists everywhere else in the interferometer. Further, this rotator field lies in the plane of the interferometer schematic of Fig. 15 and is perpendicular to the direction of propagation (k) of the neutron wave. Recall that the polarization of the neutron plays an essential role in the application of the quantum Zeno effect to enhance the efficiency of the IFM.

A neutron polarization vector $P = (P_x, P_y, P_z)$ with three rectangular components can be defined in real space in terms of two angles or, alternatively, the spinor coefficients C_+ and C_- . To determine how C_+ and C_- change under a rotation of the polarization vector P , a rotation operator can be defined in terms of the Pauli spin matrices and applied to the neutron spinor wave function. We will apply the spin rotation operator to describe how the coefficients C_{+-} of the spinor wave function transform in traversing the polarization rotator inside the interferometer.

The spin rotation device inside the interferometer is a region of uniform magnetic field orthogonal to that which exists everywhere else in the interferometer. The axis of rotation is taken to be parallel to the y axis (and perpendicular to the neutron direction of propagation along the x axis). Over some distance x in a magnetic field of strength B oriented along the y axis, the direction of the initial polarization rotates through an angle ε about the y axis. The angle of rotation ε is related to the strength of the magnetic field within and the distance traveled through the rotator (the magnetic field strength can be expressed in terms of the difference in the refractive indices for spin + and − in that field).

For that rotation from $P_i = P_{iz}$ along the z axis through an angle ε about the y axis, C_+ and C_- thus transform (denoting initial and final states by “I” and “F”, respectively) according to the following:

$$\begin{aligned} C_{F+} &= \cos(\varepsilon/2)C_{I+} - \sin(\varepsilon/2)C_{I-} \\ C_{F-} &= \sin(\varepsilon/2)C_{I+} + \cos(\varepsilon/2)C_{I-} \end{aligned} \quad (2)$$

After passing through the polarization rotator, the wave function now has nonzero values of C_+ and C_- .

The neutron wave next encounters the polarizing splitter which transmits with 100% efficiency the + spin state while reflecting the − spin state with 100% probability. For all of the other mirrors in the interferometer, we will assume the reflectivity to be unity regardless of neutron spin. Without affecting any essential aspects of the interaction-free measurement process, we can assume that the various interferometer path lengths can be adjusted such that for both k_{+-} values the argument of the exponential corresponding to the spatial phase shift is an integer multiple of 2π . Note that for this

condition to be realized for both k_{+-} over the path segments which are common to both spin + and − wavefunctions, namely between the lower gate mirror and the polarizing splitter, the magnitude of the magnetic guide field must also be adjusted such that $[(k_- - k_+) r] = 2n\pi$. We further assume that it is possible to select mirrors and splitter in conjunction with, if necessary, nonabsorbing phase shifting materials placed in the paths so that the mirrors and splitter do not introduce any net phase shifts themselves, i.e., each element has an effective $\phi = 2n\pi$.

With these simplifications, the wave function can be readily constructed at any point along the path through a circuit of the interferometer. Denoting “F” as the final wavefunction state and “ j ” the number of the cycle within the closed loop of the interferometer, the wavefunction after, say, three complete cycles can be written as

$$\begin{aligned} \psi_{Fj=3} &= [C^3 - 2CS^2t - CS^2t^2] \begin{pmatrix} 1 \\ 0 \end{pmatrix} \\ &+ t[SC^2 - S^3t + SC^2t + SC^2t^2] \begin{pmatrix} 0 \\ 1 \end{pmatrix} \end{aligned} \quad (3)$$

where

$$C = \cos(\varepsilon/2) \text{ and } S = \sin(\varepsilon/2)$$

and t is the transmission amplitude (in general a complex quantity characterized by a modulus and phase angle) of the object. Keep in mind that the wavefunction is a probability amplitude, the complex square of which represents the probability of finding the neutron at the corresponding location within the interferometer at some point in a given cycle. Note that the complex square of the wavefunction no longer equals unity if the transmission of the object in the path is less than one, which means that there is some chance that the neutron gets absorbed by the object.

In order to obtain information about the transmission $|t|^2$ of the object through this interaction-free measurement scheme, we ultimately need to let the neutron, if it has not been absorbed by the object, exit the interferometer after $j = m$ cycles through the lower gate mirror. The information about $|t|^2$ is contained in the complex square of the wavefunction. To obtain such information requires that we repeat the “experiment” (with given number of cycles m) for some number of times (one neutron at a time). The probabilities for and number of neutrons emerging in either the spin + or − state after m nominal cycles through the interferometer circuit (including the possibility of transmission through an object) are related as follows (N_j = number of neutrons originally allowed to enter the interferometer):

$$N_{F+/-} = |\psi_{F+/-}|^2 N_I = F_{+/-} N_I \quad (4)$$

where $N_F = N_{F+} + N_{F-}$ includes the numbers of neutrons detected emerging from the interferometer in the + and − spin states, respectively. If N_A is the number of neutrons which were absorbed by the object, then $N_F = N_j - N_A$. The difference D in measured numbers of spin +, N_+ , and spin −, N_- ,

neutrons is proportional to the polarization P_z of the collection or “beam” of emerging neutrons. Proper normalization is obtained by dividing this difference by the total number of neutrons emerging regardless of spin state.

We can now relate the transmission of the object $/t/2$ to the measured difference D between $+$ and $-$ neutrons (or the normalized polarization) emerging from the closed-loop interferometer after m potential cycles. This relation is, however, relatively complicated, the degree of complexity increasing with the number of cycles m , as can be seen from Eq. (3) for $m=3$. (We can, however, easily check the result for $m=3$ in the limiting cases at $t=0$ and 1. Choosing the incremental rotation angle to be $\pi/3$ (as in Ref. 34) for $m=3$, we find for $t=0$ that $N_{F+}=0.422 N_0$, $N_{F-}=0$, and $P_z=+1$ whereas for $t=1$ we have $N_{F+}=0$, $N_{F-}=N_0$, and $P_z=-1$. This is as should be expected. Similarly, for $m=1$, the expression for $T=/t/2$ reduces to N_{F-}/N_0 which is exactly the conventional expression since $N_{F+}=0$ in this case.)

Despite the complicated analytic equation for $m \geq 2$, we can, accurately and straightforwardly determine the relationship between the difference D (or polarization) and object transmission for any m numerically, through the use of a relatively simple recursive algorithm. In each cycle, the incident wavefunction is first subjected to the rotation operator, modified by the effect of transmission through the object, and, lastly, the resulting or final wave function for that cycle becomes the initial wavefunction for the subsequent cycle. We will employ such a strategy to compare the measurement of the transmission of an object done in a conventional manner with that done via the interaction-free apparatus we have been discussing here. To this end, we will make one further simplification, which, once again, does not sacrifice any of the essential behavior of the IFM method but simplifies the mathematical computations significantly. This simplification is to take the transmission t to be a real number, meaning only that the phase shift in transmission happens to be some integer multiple of 2π .

Let us then ask what value of N_I is required such that the measurement of the difference in final spin state populations, D , after m cycles through an IFM apparatus as we have described here for a particular object transmission $/t/2$ is resolvable from that for a transmission value of $/t/2 + \Delta/t/2$ (e.g., $\Delta/t/2 / /t/2 = 0.01$ or $\Delta/t/2 = 0.01 /t/2$). Using the criteria that one standard deviation is sufficient to separate two neighboring normal distributions, we can write the condition for resolution in terms of the number of neutrons N_I which must be sent through the interferometer (each to undergo, potentially, m cycles before exiting — if not absorbed by the object). In other words, the RHS of Eq. (7) below contains the number N_I of incident neutrons [see also Equation (4) above] required to enable the resolution of the two neighboring difference values D corresponding to t and $t + \delta t$ appearing on the LHS (recall that the quantity $F_{+/-}$ is defined in Eq. (4) to be the square of the final wavefunction):

$$D = N_{F+} - N_{F-}, \quad (5)$$

$$\Delta D = \text{sqrt}(N_{F+} + N_{F-}), \quad (6)$$

$$\begin{aligned} & [N_{F+}(t) - N_{F-}(t)] - [N_{F+}(t + \delta t) - N_{F-}(t + \delta t)] \\ & = \text{sqrt}[N_{F+}(t) + N_{F-}(t)], \end{aligned} \quad (7)$$

$$N_I = (F_+ + F_-)/[(F_+ - F_-) - (F_{\delta+} - F_{\delta-})]^2, \quad (8)$$

where we have assumed that N_I for $D(t)$ is negligibly different than that for $D(t + \delta t)$.

We now have the relationships we need to ask what number of neutrons N_I must be run through the IFM device, configured for m cycles, to be able to measure a semitransparent object’s transmission $T=/t/2$ with an accuracy $\Delta T = \Delta/t/2$. From N_I we can also retrieve N_A , the number of neutrons actually absorbed by the object in the process. However, before presenting and discussing results of the computations outlined above for an IFM, let us first express the uncertainty associated with a conventional measurement of the transmission of neutrons through an object so that a comparison may also be made.

D. Conventional transmission measurement

The formulas for a conventional transmission measurement and its corresponding uncertainty are given by the following [$/t_c/2 = T_c$ is the conventional transmission where N_F and N_I are the numbers of transmitted (final) and incident neutrons, respectively]:

$$|t_c|^2 = N_F/N_I = T_c, \quad (9)$$

$$N_I = T_c(1 + T_c)/(\Delta T_c)^2. \quad (10)$$

Note that just as in the IFM case, we can ask what number of incident neutrons N_I are required to achieve a given level of accuracy in the measurement of the transmission $/t/2$, for example, as specified by the fractional uncertainty $\Delta T / T = \Delta/t/2 / /t/2$.

E. Interaction-free versus conventional transmission measurement

The results of the calculations described in the two preceding sections are summarized in the following three Figs. 16, 17, and 18.

We can check the IFM expressions analytically for N_F and related quantities in the limiting cases at $t=0$ and 1. For example, choosing the incremental rotation angle to be $\pi/3$ (as in Ref. 34) for $m=3$, we find for $t=0$ that $N_{F+}=0.422 N_0$, $N_{F-}=0$, and $P_z=+1$ whereas for $t=1$ we have $N_{F+}=0$, $N_{F-}=N_0$, and $P_z=-1$. In the conventional transmission measurement case, for $T_c=1.0$, $N_{Ic}=20,000$. and for $T_c=0.005$ (first point in Figs. 16 and 17, and 18), $N_{Ic}=2,010,000$. (using the appropriate equation given above for the conventional transmission measurement case).

In summary, it appears that insofar as the number of neutrons needed for a measurement of the transmission with a given accuracy are concerned, the IFM technique does not outperform the conventional measurement method for all values of the object’s transmission. The IFM behaves similarly regarding the number of neutrons absorbed by the

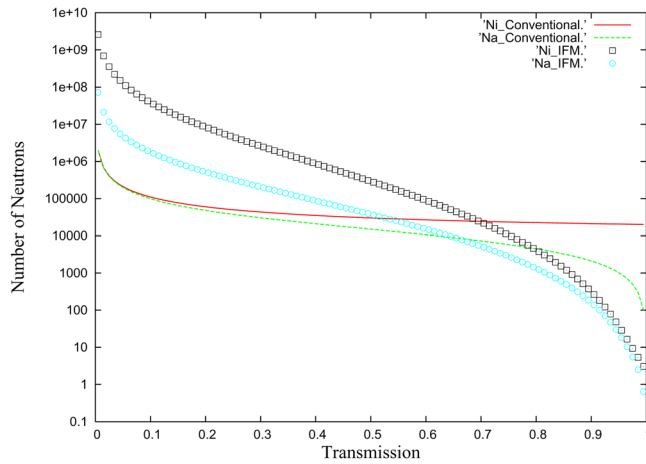


FIG. 16. (Color online) Number of neutrons N_I (square symbols), as a function of transmission through a semi-transparent object, required to achieve an uncertainty of 1% in the transmission ($\Delta T / T = 0.01$) for $m = 100$ cycles through the interferometer in an interaction-free measurement as described in the text. The circles indicate the corresponding number of neutrons absorbed by the semitransparent object in the process. The incremental turn angle ε of the polarization in each of the m cycles is given by the prescription of Kwiat *et al.*¹¹ to be π / m . For comparison, the number of incident neutrons required and associated number absorbed by the object for a conventional transmission experiment are given by the solid and dashed lines, respectively. Interestingly, IFM is markedly inferior to conventional measurement up to transmission values of about 0.65 – insofar as the number of incident neutrons required and corresponding number absorbed are concerned. Note, however, that at a transmission approaching zero, the ratio of $N_I/N_A > 10$ for an IFM whereas it is unity for a conventional measurement.

object. For relatively low values of the transmission of the object, the IFM method does not appear to be an advantage. Unfortunately, it is for these low values of the transmission where the conventional measurement technique also requires the most incident and absorbed numbers of neutrons to achieve a given accuracy. (For measurements of an object's reflectivity, the lower the reflectivity, the more neutrons

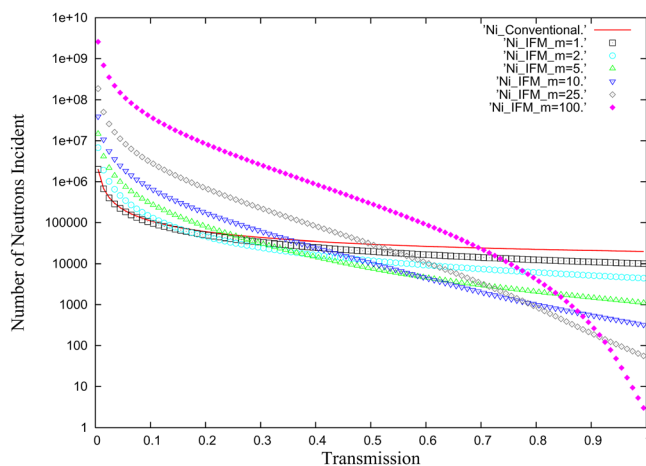


FIG. 17. (Color online) Number of incident neutrons N_I , as a function of transmission through a semi-transparent object, required to achieve 1% fractional uncertainty in the transmission ($\Delta T / T$). The solid line is for the conventional measurement case whereas the results for the interaction-free approach are given for various values of cycles m , as indicated in the legend in the upper right-hand corner of the plot. In terms of the number of neutrons needed, the efficiency of the IFM technique varies as a function of the number of cycles m at a given transmission value.

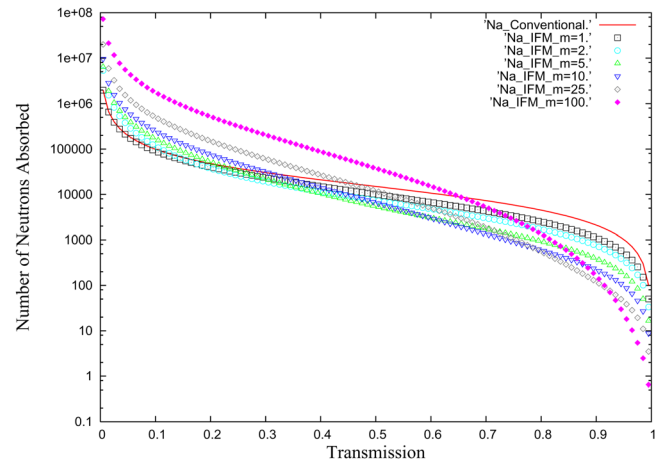


FIG. 18. (Color online) Number of neutrons absorbed N_A , as a function of transmission through a semi-transparent object, in the process of achieving a 1% fractional uncertainty in the transmission ($\Delta T / T$). The solid line is for the conventional measurement case whereas the results for the interaction-free approach are given for various values of cycles m , as indicated in the legend in the upper right-hand corner of the plot. Insofar as number of neutrons absorbed by the object is concerned, the efficiency of the IFM technique varies as a function of the number of cycles m at a given transmission value.

would be needed.) For transmission values approaching unity, on the other hand, IFM does appear to offer some advantage over a conventional measurement. However, even for values of the transmission where the IFM technique could be of advantage over conventional methods of measurement, there remains the formidable task, for neutrons and x-rays at least, of finding a practical method of performing the inter-action free measurement (note that most of the experimental realizations of IFM done thus far have been for optical wavelength photons).

VI. CONCLUSIONS

In addition to the more obvious (but still important) elements affecting the sensitivity of specular neutron reflectometry as a probe of thin film nanostructure — such as source strength, incoherent scattering background, and optimization of instrumental Q resolution — several other factors can have a significant impact. We have discussed a number of these, including the crucial role that phase information plays in obtaining unambiguous SLD depth profiles — not only through the phase-inversion process itself, but by making it possible to obtain information regarding the in-plane homogeneity of the sample. Phase-inversion also enables accurate, quantitative analysis of the uncertainty associated with a SLD profile deduced from actual NR data which possesses statistical noise and covers only a finite range of Q . We also discussed how interfacial roughness further limits the spatial resolution which can be achieved.

As an illustration of the sensitivity of NR in a current application in materials science, a study involving an organic photovoltaic film system was examined. In this investigation of the film's morphology, phase-inversion methods were applied to determine the SLD profile and the distribution of two essential molecular components. The SLD so determined

is unequivocal to within the degree allowed by the statistical uncertainty and Q range of the measured reflectivity data. Such nanometer scale structural information could not have been obtained by any other means currently available, including electron microscopy techniques.

Finally, the possible application of the quantum phenomenon of “interaction-free” measurement to neutron reflectometry was considered. A measuring apparatus such as an interferometer can be viewed as an intricate but well-defined sample environment, one that is more complicated than that created by a simple reference medium surrounding the sample, as is presently employed in the phase-inversion method. The possibility of whether some IFM of neutron transmission through (or reflection from) an object within such a device could be performed with better efficiency at a given accuracy than by conventional means was considered. Although it appears that for a certain range of transmission (reflectivity) values an IFM might be advantageous, there remains the not insignificant problem of constructing a practical instrument with which to perform such a measurement. Nonetheless, it can be argued that the question of how IFM phenomena might be profitably applied to NR warrants further study.

APPENDIX: ALTERNATIVE DESCRIPTION OF THE SENSITIVITY OF THE INTERACTION-FREE MEASUREMENT

We give an alternative derivation of the IFM spin polarization device discussed above, which some readers may find helpful. As in the main text, we assume here that spatially dependent phases have been chosen to cancel out, so that the instrument acts solely on spin.

As mentioned in the text, for analytical purposes, the cyclic arrangement for the measurement may be envisioned as a linear arrangement in which each cycle is a binary choice stage, and a set of cycles corresponds to a “piecewise continuous” set of consecutive stages. The input to the device is characterized by the spinor (we use arrows here, instead of $+/-$)

$$\psi_0 = \begin{pmatrix} \psi_{0\uparrow} \\ \psi_{0\downarrow} \end{pmatrix}$$

and the output after n cycles by the spinor

$$\psi_n = \begin{pmatrix} \psi_{n\uparrow} \\ \psi_{n\downarrow} \end{pmatrix} = M^n \begin{pmatrix} \psi_{0\uparrow} \\ \psi_{0\downarrow} \end{pmatrix}, \tag{A1}$$

where M is the single-stage “transfer matrix”,

$$M = \begin{pmatrix} \cos \theta & -\sin \theta \\ t \sin \theta & t \cos \theta \end{pmatrix} \tag{A2}$$

$\theta = \pi / 2n = \varepsilon / 2$ is the spinor rotation angle (half the spin rotation angle) for each stage, and t is the sample transmission. The top row of M corresponds to paths that are transmitted by the beam splitter and thus do not “see” the sample, while the bottom row accounts for the possibility of paths reflected by the splitter to the leg of the instrument contain-

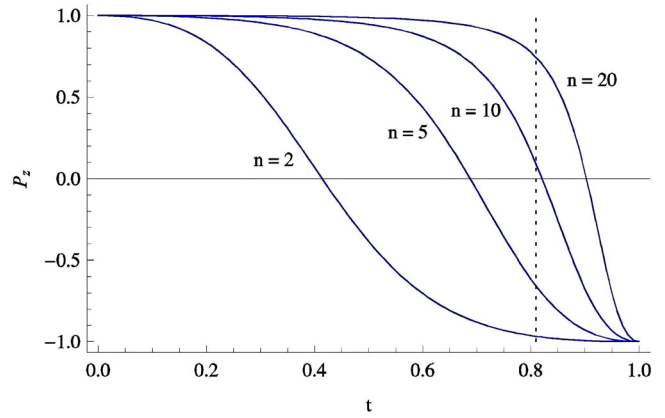


FIG. 19. (Color online) $P_z(n, t)$ vs t for several n , showing the evolution of the sigmoidal shape with n . The dotted line shows $t = 0.81$; $n = 10$ is a good choice for measuring this value with IFM.

ing the sample. Thus for $t = 1$ (perfect transmitter), M^n simply rotates the input spinor by π . For $t = 0$ (perfect absorber), $\psi_{n\uparrow} = (\cos \theta)^n \psi_{0\uparrow}$ and $\psi_{n\downarrow} = (\sin \theta)^n \psi_{0\downarrow}$, so that $\psi_{n\downarrow}$ goes to zero and $\psi_{n\uparrow} \sim [1 - O(n^{-1})] \psi_{0\uparrow}$ as n approaches infinity. That is, as t goes to zero, the device becomes a perfect polarizer—for any neutrons that emerge from it.

For a polarized incident neutron, the output polarization along the z axis after n cycles is

$$P_z(n, t) = \frac{|\psi_{n\uparrow}|^2 - |\psi_{n\downarrow}|^2}{|\psi_{n\uparrow}|^2 + |\psi_{n\downarrow}|^2} = p_{n\uparrow} - p_{n\downarrow} \tag{A3}$$

as in the text. In Fig. 19 we show $P_z(n, t)$ for several n and take notice of its sigmoidal shape, the “knee” of which sharpens and moves toward t approaching 1 with increasing n . In both Figs. 19 and 20, we take $\psi_{0\uparrow} = 1$ and $\psi_{0\downarrow} = 0$.

In Fig. 20 we show the effect of this shape on the determination of t from measured polarizations using N neutrons, simulated by using the binomial probability function $B(p, N)$

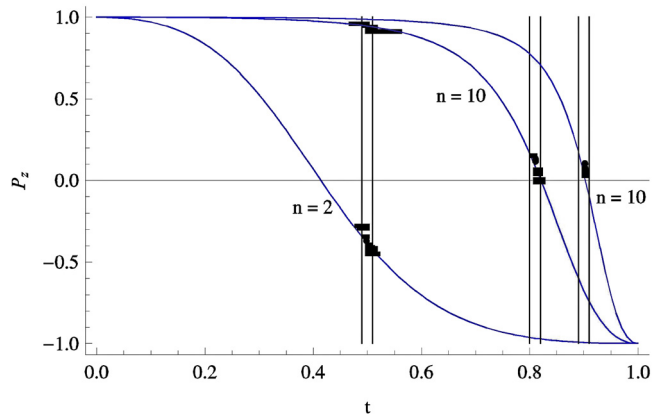


FIG. 20. (Color online) Determinations of t by IFM for several $t - n$ pairs, using 10 runs, each with 200 neutrons. Thick horizontal lines terminate on measured $t -$ values for each P_z measurement, simulated using the Binomial probability distribution appropriate to the given $t - n$ pairs (see text.) Pairs of vertical lines demarcate $t \pm 0.01$ for comparison with the actual spread. In particular, for the $0.9 - 20$ pair, all the IFM variations of t lie well within the std. err. for P_z .

for the theoretical up and down probabilities $p = p_{n\uparrow}$ and $p = p_{n\downarrow}$ from Eq. (A3). It is easy to see that when the number of cycles n is chosen to make the knee of the sigmoid fall near the actual value of t , a position corresponding to $P_z \sim 0$, the measurement of t is relatively insensitive to the statistical $1/\sqrt{N}$ fluctuations of the polarizations measured in n cycles of the instrument; i.e., the *sensitivity to t* is high. In fact, we see that then the spread in measured t is comparable to or less than $t \pm 0.01$ for sufficiently large n and t not too large or small.

On the other hand, as the edge of the sigmoid broadens or moves away from the location of actual t , fluctuations in measured t can significantly exceed fluctuations in measured P_z . In particular, for values of t near zero (strong absorbers), there is no value of n which places t at a sharp edge of $P_z(n, t)$. Roughly speaking, this can be stated in the following way. We “know” a strong absorber is present, because few neutrons emerge from the instrument, all with nearly the incident polarization, but we cannot accurately measure $t \sim 0$ because *too* few neutrons emerge for the purpose, and the larger we make n , the worse this incommensurability gets. The importance of a “good” $t - n$ pair is clearly illustrated in Fig. 20 by comparing the cases $n = 2$ and 10 for $t = 0.5$.

A simple argument may help to bring out the character of the sensitivity that was derived in detail in the main text. Let P stand for P_z , and begin with the trivial identity $dP = (dP/dt)dt$. Then, $dt = dP / (dP / dt)$ goes to $|\Delta t| \sim |\Delta P| / |dP / dt|$ where Δt and ΔP refer now to *measured* quantities, but dP/dt signifies the slope of the theoretical sigmoidal polarization function. Then it is obvious that the sensitivity of the instrument varies inversely with the slope of P near the true value of t . Sensitivity to t is highest when n is chosen to make t intercept P_z near the center of the sigmoidal knee, corresponding to $P_z \sim 0$ for a completely polarized incident beam.

ACKNOWLEDGMENTS

We (CFM and EC) acknowledge interesting and productive discussions with Ron Cappelletti on the subject of IFM.

- ¹M. R. Fitzsimmons, S. D. Bader, J. A. Borchers, G. P. Felcher, J. K. Furdyna, A. Hoffman, I. K. Schuller, T. C. Schulthess, S. K. Sinha, M. F. Toney, D. Weller, and S. Wolf, *J. Magn. Magn. Mater.* **271**, 1369 (2004).
- ²J. Penfold and R. K. Thomas, *J. Phys.: Condens. Matter* **2**, 1369 (1990).
- ³T. P. Russell, *Mater. Sci. Rep.* **5**, 171 (1990).
- ⁴C. F. Majkrzak, ACA RefleXions **Summer No.2**, 12 (2007).
- ⁵S. Krueger, C. W. Meuse, C. F. Majkrzak, J. A. Dura, N. F. Berk, M. Tarek, and A. L. Plant, *Langmuir* **17**, 511 (2001).

- ⁶C. F. Majkrzak, N. F. Berk, and U. A. Perez-Salas, *Langmuir* **19**, 7796 (2003).
- ⁷N. F. Berk and C. F. Majkrzak, *Langmuir* **25**, 4132 (2009).
- ⁸M. Renninger, *Z. Phys.* **158**, 417 (1960).
- ⁹R. H. Dicke, *Am. J. Phys.* **49**, 925 (1981).
- ¹⁰A. Elitzur and L. Vaidman, *Found. Phys.* **23**, 987 (1993).
- ¹¹P. Kwiat, H. Weinfurter, T. Herzog, A. Zeilinger and M. A. Kasevich, *Phys. Rev. Lett.* **74**, 4763 (1995).
- ¹²H. Hauptman, *Science* **233**, 178 (1986).
- ¹³N. F. Berk and C. F. Majkrzak, *Phys. Rev. B* **51**, 11296 (1995).
- ¹⁴C. F. Majkrzak and N. F. Berk, *Physica B* **336**, 27 (2003).
- ¹⁵K. Chadan and P. C. Sabatier, *Inverse Problems in Quantum Scattering Theory* (Springer, New York, 1989).
- ¹⁶N. F. Berk and C. F. Majkrzak, *J. Phys. Soc. Jpn.* **65**, 107 (1996).
- ¹⁷P. E. Sacks, *Wave Motion* **18**, 21 (1993).
- ¹⁸C. F. Majkrzak and N. F. Berk, *Phys. Rev. B* **52**, 10827 (1995).
- ¹⁹V. O. deHaan, A. A. van Well, S. Adenwalla, and G. P. Felcher, *Phys. Rev. B* **52**, 10831 (1995).
- ²⁰C. F. Majkrzak and N. F. Berk, *Phys. Rev. B* **58**, 15416 (1998). (Erratum *Phys. Rev. B* **60**, 16211.)
- ²¹R. Lipperheide, J. Kasper, and H. Leeb, *Physica B* **248**, 366 (1998).
- ²²J. Kasper, H. Leeb, and R. Lipperheide, *Phys. Rev. Lett.* **80**, 2614 (1998).
- ²³A. Schreyer, C. F. Majkrzak, N. F. Berk, H. Gruell, and C. Han, *J. Phys. Chem. Solids* **60**, 1045 (1999).
- ²⁴C. F. Majkrzak, N. F. Berk, P. Kienzle, and U. Perez-Salas, *Langmuir* **25**, 4154 (2009).
- ²⁵M. K. Sanyal, S. K. Sinha, A. Gibaud, K. G. Huang, B. L. Carvalho, M. Rafailovich, J. Sokolov, X. Zhao, and W. Zhao, *Europhys. Lett.* **21**, 691 (1993).
- ²⁶H. Leeb, H. Groetz, J. Kasper, and R. Lipperheide, *Phys. Rev. B* **63**, 045414-1 (2001).
- ²⁷C. F. Majkrzak, N. F. Berk, S. Krueger, J. A. Dura, M. Tarek, D. Tobias, V. Silin, C. W. Meuse, J. Woodward, and A. L. Plant, *Biophys. J.* **79**, 3330 (2000).
- ²⁸U.A. Perez-Salas, K. Faucher, C. F. Majkrzak, N. F. Berk, E. Chaikof, and S. Krueger, *Langmuir* **19**, 7688 (2003).
- ²⁹C. F. Majkrzak, N. F. Berk, V. Silin, and C. W. Meuse, *Physica B* **283**, 248 (2000).
- ³⁰S. Krueger and C. F. Majkrzak, “Adsorption of an alkane thiol hybrid bilayer membrane on Au under various flow conditions,” (unpublished).
- ³¹D. J. McGillivray, G. Valincius, F. Heinrich, J. W. F. Robertson, D. J. Vanderah, W. Febo-Ayala, I. Ignatjev, M. Loesche, and J. Kasianowicz, *Biophys. J.* **96**, 1547 (2009).
- ³²J. W. Kiel, B. J. Kirby, C. F. Majkrzak, B. B. Maranville, and M. E. Mackay, *Soft Matter* **6**, 641 (2010).
- ³³J. W. Kiel, M. E. Mackay, B. J. Kirby, B. B. Maranville, and C. F. Majkrzak, *J. Chem. Phys.* **133**, 074902-1 (2010).
- ³⁴P. G. Kwiat, *Phys. Scr.* **T76**, 115 (1998).
- ³⁵P. Kwiat, H. Weinfurter, and A. Zeilinger, *Sci. Am.* **November**, 72 (1996).
- ³⁶P.G. Kwiat, A.G. White, J.R. Mitchell, O. Nairz, G. Weihs, H. Weinfurter, and A. Zeilinger, *Phys. Rev. Lett.* **83**, 4725 (1999).
- ³⁷T. Tsegaye, E. Goodbar, A. Karlsson, G. Bjork, M.Y. Loh, and K. H. Lim, *Phys. Rev. A* **57**, 3987 (1998).
- ³⁸W. P. Putnam and M. F. Yanik, *Phys. Rev. A* **80**, 040902-1 (2009).
- ³⁹Ju-Seog Jang, *Phys. Rev. A* **59**, 2322 (1999).
- ⁴⁰G. Krenn, J. Summhammer, and K. Svozil, *Phys. Rev. A* **61**, 052102-1 (2000).
- ⁴¹G. Mitchison and S. Massar, *Phys. Rev. A* **63**, 032105-1 (2001).